

Experiments and SPICE simulations of double MgO-based perpendicular magnetic tunnel junction

Qiuyang Li(李求洋), Penghe Zhang(张蓬鹤), Haotian Li(李浩天), Lina Chen(陈丽娜), Kaiyuan Zhou(周恺元), Chunjie Yan(晏春杰), Liyuan Li(李丽媛), Yongbing Xu(徐永兵), Weixin Zhang(张卫欣), Bo Liu(刘波), Hao Meng(孟浩), Ronghua Liu(刘荣华), and Youwei Du(都有为)

Citation: Chin. Phys. B, 2021, 30 (**4**): 047504. DOI: 10.1088/1674-1056/abdea2
Journal homepage: http://cpb.iphy.ac.cn; http://iopscience.iop.org/cpb

What follows is a list of articles you may be interested in

Enhanced spin-orbit torque efficiency in $Pt_{100-x}Ni_x$ alloy based magnetic bilayer

Congli He(何聪丽), Qingqiang Chen(陈庆强), Shipeng Shen(申世鹏), Jinwu Wei(魏晋武), Hongjun Xu(许洪军), Yunchi Zhao(赵云驰), Guoqiang Yu(于国强), and Shouguo Wang(王守国)

Chin. Phys. B, 2021, 30 (**3**): 037503. DOI: 10.1088/1674-1056/abe3f4

Field-induced N'eel vector bi-reorientation of a ferrimagnetic insulator in the vicinity of compensation temperature

Peng Wang(王鹏), Hui Zhao(赵辉), Zhongzhi Luan(栾仲智), Siyu Xia(夏思宇), Tao Feng(丰韬), and Lifan Zhou(周礼繁)

Chin. Phys. B, 2021, 30 (**2**): 027501. DOI: 10.1088/1674-1056/abbbef

Spin torque nano-oscillators with a perpendicular spin polarizer

Cuixiu Zheng(郑翠秀), Hao-Hsau Chen(陈浩轩), Xiangli Zhang(张祥丽), Zongzhi Zhang(张宗芝), Yaowen Liu(刘要稳)

Chin. Phys. B, 2019, 28 (**3**): 037503. DOI: 10.1088/1674-1056/28/3/037503

Strong anti-strain capacity of CoFeB/MgO interface on electronic structure and state coupling

Fei Guo(郭飞), Yaping Wu(吴雅苹), Zhiming Wu(吴志明), Ting Chen(陈婷), Heng Li(李恒), Chunmiao Zhang(张纯淼), Mingming Fu(付明明), Yihong Lu(卢奕宏), Junyong Kang(康俊勇)

Chin. Phys. B, 2018, 27 (**1**): 017502. DOI: 10.1088/1674-1056/27/1/017502

Perpendicular magnetic tunnel junction and its application in magnetic random access memory

Liu Hou-Fang, Syed Shahbaz Ali, Han Xiu-Feng

Chin. Phys. B, 2014, 23 (**7**): 077501. DOI: 10.1088/1674-1056/23/7/077501

Experiments and SPICE simulations of double MgO-based perpendicular magnetic tunnel junction*

Qiuyang Li(李求洋)[1], Penghe Zhang(张蓬鹤)[1], Haotian Li(李浩天)[2,†], Lina Chen(陈丽娜)[2,3], Kaiyuan Zhou(周恺元)[2], Chunjie Yan(晏春杰)[2], Liyuan Li(李丽媛)[2], Yongbing Xu(徐永兵)[4], Weixin Zhang(张卫欣)[5], Bo Liu(刘波)[6], Hao Meng(孟浩)[6], Ronghua Liu(刘荣华)[2,‡], and Youwei Du(都有为)[2]

[1] *China Electric Power Research Institute, Beijing* 100192, *China*
[2] *School of Physics, Nanjing University, Nanjing* 210093, *China*
[3] *School of Science, Nanjing University of Posts and Telecommunications, Nanjing* 210023, *China*
[4] *School of Electronics Science and Engineering, Nanjing University, Nanjing* 210093, *China*
[5] *State Grid Tianjin Electric Power Company, Tianjin* 300384, *China*
[6] *Key Laboratory of Spintronics Materials, Devices and Systems of Zhejiang Province, Zhejiang* 311300, *China*

(Received 29 December 2020; revised manuscript received 19 January 2021; accepted manuscript online 22 January 2021)

We investigate properties of perpendicular anisotropy magnetic tunnel junctions (pMTJs) with a stack structure MgO/CoFeB/Ta/CoFeB/MgO as the free layer (or recording layer), and obtain the necessary device parameters from the tunneling magnetoresistance (TMR) vs. field loops and current-driven magnetization switching experiments. Based on the experimental results and device parameters, we further estimate current-driven switching performance of pMTJ including switching time and power, and their dependence on perpendicular magnetic anisotropy and damping constant of the free layer by SPICE-based circuit simulations. Our results show that the pMTJ cells exhibit a less than 1 ns switching time and write energies < 1.4 pJ; meanwhile the lower perpendicular magnetic anisotropy (PMA) and damping constant can further reduce the switching time at the studied range of damping constant $\alpha < 0.1$. Additionally, our results demonstrate that the pMTJs with the thermal stability factor $\simeq 73$ can be easily transformed into spin-torque nano-oscillators from magnetic memory as microwave sources or detectors for telecommunication devices.

Keywords: magnetic tunnel junctions, magnetic tunnel junction (MTJ) model, switching time, spin torque nano-oscillator

PACS: 75.47.–m, 75.70.–i, 75.75.–c, 85.75.–d **DOI:** 10.1088/1674-1056/abdea2

1. Introduction

Spintronics as an emerging technology began from discoveries of giant magnetoresistance (GMR) and tunneling magnetoresistance (TMR) effects in the 1980s. One of the main applications of these magnetoresistive effects is in magnetic field sensors, e.g., in hard disk drive read heads and biosensors. There are four main types of magnetic transducers: Hall effect, anisotropic magnetoresistance (AMR), GMR, and TMR. Compare to Hall element with large power consumption and poor linearity, the AMR element has a much higher sensitivity, but a narrower linear operating range. The magnetoresistance (MR) ratios of conventional AMR and GMR elements are about 3 % and 12% at room temperature, respectively, while the TMR element can be over 200%,[1] which indicates higher sensitivity. Besides the much higher sensitivity, the TMR element has better temperature stability, low power consumption, and a wider linear range relative to ARM and GMR sensing elements. This is why the TMR element is utilized as a highly-sensitive reading element in hard dish drive these days.[2,3]

On the other hand, the functionalities of spintronic devices have made significant progress in magnetic memory, logic devices, and radio-frequency electronics in the last two decades[4] following the discovery of spin-transfer torque (STT) effect enabling electronic control of nanomagnetic systems.[5,6] The spin current-driven STT can not only change the static magnetic configuration by generating the effective magnetic field,[7–9] but also can result in the excitation of coherent dynamical magnetization states by compensating the dynamical damping in magnetic systems.[9,10] Intense ongoing efforts in the former are focused on exploring STT-MTJ including to achieve higher density integration of MTJ cells for magnetic random access memory (MRAM),[11] meanwhile keep high thermal stability and low power consumption.[2,4,12–15] Many of these challenges are closely related to the fact that the current required to switch the magnetization is proportional to the energy barrier separating the two states. At the same time, the thermal stability of the device is also proportional to the magnetic anisotropy energy. Therefore, a higher energy barrier will improve the nonvolatil-

*Project supported by State Grid Corporation of China under the 2018 Science and Technology Project of State Grid Corporation: Research on electromagnetic measurement technology based on EIT and TMR (Grant No. JL71-18-007).

†Corresponding author. E-mail: lht_phy@smail.nju.edu.cn
‡Corresponding author. E-mail: rhliu@nju.edu.cn

© 2021 Chinese Physical Society and IOP Publishing Ltd

ity, but it also requires a higher current to flip states. In the past ten years, researchers have theoretically proposed and experimentally verified various approaches to solve these challenges such as to temporarily lower the energy barrier right before applying an STT current by using voltage-controlled magnetic anisotropy (VCMA) effect[16–19] or heating effect, to improve the nonvolatility by incoming the anisotropy fields due to the interlayer or interfacial exchange coupling between magnetic layers,[20–22] and to further reduce the switching current by combining STT and spin–orbit torque (SOT) in three-terminal MTJ structure.[23] For the spin-torque driven dynamical magnetization, many studies are focused on investigating the relationship among the coherence of the dynamical states in spin-torque nano-oscillators (STNOs),[9,10,24] the magnetic properties, and the layout of magnetic nanostructures with the goal of achieving the optimized characteristics of STNOs for the specific applications in radio-frequency electronics, spin wave-based devices, and neuromorphic computing.[25,26]

In this paper, we first investigate properties of the pMTJ cell with a stack structure MgO/CoFeB/Ta/CoFeB/MgO as the free layer (or recording layer), and obtain the necessary device parameters from the TMR vs. field loops and current-driven magnetization switching experiments. Additionally, we study the STT-pMTJ switching performance including switching time and power, and their dependence on the perpendicular magnetic anisotropy and damping constant of the free layer, as well as pMTJ-based STNO dynamics performance by using SPICE model based on the experimentally obtained device parameters. This paper is organized as follows. First, the stacked structure of STT-pMTJ and the experimental results of static magnetization switching driven by magnetic field and currents are shown in Section 2. Next, Section 3 introduces the background, key physical effects involved in our studied STT-pMTJ cell, and the SPICE model used in this paper. Section 4 investigates the effect of material parameters on the switching dynamics performance. Finally, conclusions are summarized in Section 5.

2. Experimental results of STT-pMTJ

Since its greater thermal stability than that of the in-plane magnetized MTJ, the perpendicularly magnetized MTJ structure has been widely adopted to build MRAM cells, magnetic field sensors, and STNOs for microwave generators or detectors. Given perpendicular magnetic anisotropy (PMA) advantages, various PMA materials, such as rare-earth transition metal amorphous alloy layer, [Co/(Pt,Pd)] multilayers, and CoFeB/MgO frames, have been widely investigated for the past decade. Among these PMA materials, the CoFeB/MgO/CoFeB frames were intensively studied for the development of practical devices due to their large TMR ratio.[27] Here, we adopted pMTJ cells with the following stacks of buffer/SAF/spacer/CoFeB(1)/MgO(1.4)/CoFeB(1)/Ta(0.4) /CoFeB(1.6)/MgO(1)/capping layer (thicknesses in nm) to enhance further PMA, as well as the thermal stability factor by utilizing the double-interface structure as the recording layer (or free layer) instead of the single-interface structure, as shown in the inset of Fig. 1(a). The SAF represents Co/Pt multilayer based synthetic ferrimagnetic reference layer with a minimum stray field on the recording layer.[21] The multilayer was subsequently patterned into circle-shaped nano-pillars with a diameter of less than 100 nm. TMR hysteresis loops of these pMTJ nano-pillars were investigated substantially under out-of-plane magnetic fields at a small bias current of 1 μA. Figure 1(a) shows the representative minor TMR hysteresis loop corresponding to magnetization switching of the free layer in the MTJ cell. The well defined square-shaped TMR hysteresis loop indicates that the studied MTJ cell has a strong PMA for both free layer (FL) and reference layer (RL). The high resistance state R_{AP} and low resistance state R_{P} correspond to the antiparallel (AP) and parallel (P) alignment of magnetization of RL and FL, respectively, as shown in Fig. 1(a). The TMR ratio is defined as $\mathrm{TMR} = 100 \times (R_{\mathrm{AP}} - R_{\mathrm{P}})/R_{\mathrm{P}}$. A TMR ratio of as high as 188% can be achieved at room temperature, indicating good quality of pMTJ. Additionally, the TMR hysteresis loop was offset to 1.17 kOe from the origin of the applied magnetic field, indicating that FL suffers the influence of the stray field as well as the possible interlayer exchange coupling between FL and RL. Similar results were observed in devices with other sizes and did not show a clear dependence of TMR ratio on their resistance-area product (RA) ($< 10\ \Omega \cdot \mu\mathrm{m}^2$), indicating that our pMTJ cell array has a very good uniformity and may achieve high-performance, low energy STT-pMRAM.

To investigate STT-driven magnetization switching characteristics of the MTJ with strong PMA, the current-driven magnetization switching experiments were performed at room temperature. Figure 1(b) shows the representative resistance vs. current (R–I) curves of the pMTJ obtained by scanning dc current at various out-of-plane bias magnetic fields. Positive bias current corresponds to electrons flowing from the reference layer to the free layer and thus favors parallel alignment of magnetization of FL and RL. The value of high resistance R_{AP} shows an obvious decrease with increasing amplitude of bias current for all R–I curves. Additionally, the critical current $I_{\mathrm{c}}^{\mathrm{AP}\longrightarrow\mathrm{P}}$ (from AP to P state) is smaller (larger) than $I_{\mathrm{c}}^{\mathrm{P}\longrightarrow\mathrm{AP}}$ (from P to AP state) when applied a negative (positive) bias magnetic field. The strong current dependent TMR ratio and field-dependent critical currents (I_{c}) behaviors observed in Fig. 1(b) are related to bias voltage and temperature-dependent spin polarizability of materials, also consistent with the previous reports of typical STT-induced magnetization switching

in pMTJ. The average critical switching current density J_{c0} of 5 MA/cm^2 at zero external field is comparable to other reported MgO-based MTJs. Furthermore, the spin transfer efficiency $\eta \sim 0.29$ and the spin polarization factor $P_0 \sim 70\%$ as device parameters used in the SPICE model also can be estimated from the experimental data above.

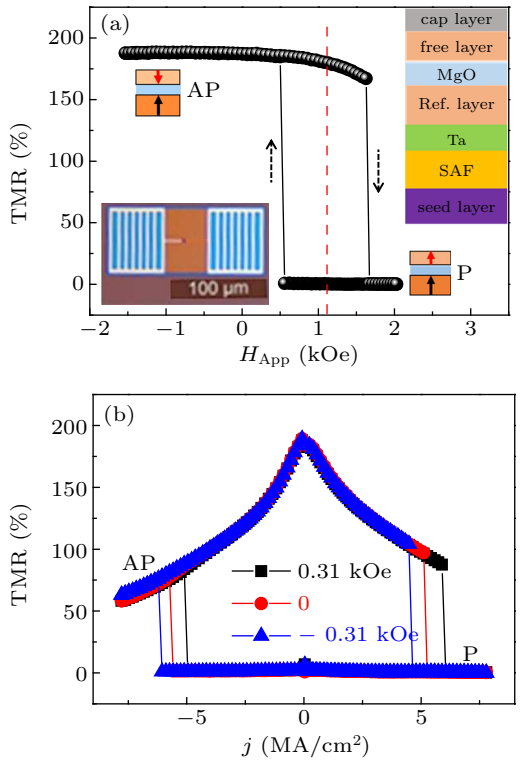


Fig. 1. TMR loops of MTJ cell with 60 nm diameter. (a) Minor TMR vs. H_{App} loop corresponding to the magnetization switching of the free layer (FL). The vertical dashed line represents the shift field owing to the stray field, as well as the possible interlayer exchange coupling. The dashed arrows represent the direction of magnetization switching from parallel (P) to antiparallel (AP) states, or in reverse. The magnetization configuration of FL and the reference layer (RL) are marked as the solid arrows in the two rectangles, respectively. The left bottom inset is the optical image of the measurement structure of one single MTJ cell. The right top inset is the physical multilayer stacks structure of an MTJ cell. (b) TMR vs. bias current (voltage) loops under the different external fields of −0.31 kOe, 0, and 0.31 kOe, respectively.

3. Background and key physics

3.1. Perpendicular magnetic anisotropy

As mentioned before, studies showed that a PMA-based MTJ has a lower switching current than an in-plane magnetic anisotropy based MTJ with the same thermal stability factor Δ.[15] In studied MgO/CoFeB/Ta/CoFeB/MgO-based pMTJ systems, the perpendicular magnetic anisotropy originates from the interfacial anisotropy of both CoFeB–Ta and CoFeB–MgO interfaces. For a magnetic system, the effective perpendicular anisotropy field ($H_{K\perp eff}$) can be generally expressed as

$$H_{K\perp eff} = H_{K\perp} - H_{dz} = 2K_{\perp}/M_S - 4\pi N_{dz} M_S, \quad (1)$$

where $H_{K\perp}$ is the perpendicular anisotropy field related to PMA, H_{dz} and N_{dz} are the z-axis component of the demagnetization field H_d and corresponding geometry-dependent demagnetization coefficient, M_S is the saturation magnetization of the magnetic free layer. For interface PMA (iPMA) system, the PMA constant $K_{\perp}$ can be expressed as $K_i/t_F = 2\pi M_S^2 t_C/t_F$, where K_i is the interfacial anisotropy energy density, t_F is the thickness of the magnetic free layer, and t_C is its critical thickness where the magnetic system has a perpendicular magnetization at zero field.

3.2. Voltage-controlled magnetic anisotropy effect

In recent years, many experimental and theoretical studies have shown that voltage-controlled magnetic anisotropy (VCMA) can be induced by the charge accumulation at the interface of ferromagnetic materials owing to an applied electric field.[16–18] Since the accumulated charge screens the external electric field in the region within a few monatomic layers of the metal–barrier interface, the VCMA is also closely related to the interface. The relationship between the gate-voltage and iPMA can be modeled by an empirical formula as follows:

$$\Delta K_i = K_i(V) - K_i(V=0) = -\xi V_F/t_b, \quad (2)$$

where ξ is the VCMA coefficient that represents the sensitivity between the magnetic anisotropy and the applied electric field, and t_b is the thickness of the oxide barrier layer MgO. Additionally, the energy barrier of the free layer between two magnetization configurations can be represented as $E_b = \mu_0 M_S V_F H_K/2$, where V_F is the volume of the free layer, M_S and H_K are the saturation magnetization and the anisotropy magnetic field, respectively. Therefore, the voltage-controlled iPMA $H_{K\perp eff}$ can modulate the energy barrier E_b, resulting in the reduction of the critical switching current, even directly switching the magnetization of the free layer. As mentioned before, the thermal stability factor Δ is a critical parameter determining the data retention capability of MRAM, which is defined as the energy barrier E_b of the recording layer normalized to the thermal energy $k_B T$, where k_B is Boltzmann's constant, and T is the absolute temperature.

3.3. Spin transfer torque

Spin transfer torque effect describes the transfer of angular momentum from electrons spin polarized by the fixed magnetic layer (also named as the polarized layer) and delivered in the form of torque to switch the magnetization of the free layer in an MTJ or spin valve.[5,6] The direction of the generated torque is determined by the direction of the applied electric current perpendicularly passing through the devices and the magnetization of the polarized layer. Therefore, instead of the external field switching, a bidirectional current can control a bidirectional magnetization switching of the free layer in an STT-MTJ cell with a fixed magnetic layer as the polarized layer. The intrinsic threshold current density J_{c0} is an important parameter that characterizes STT magnetization

switching in STT-MRAM. The threshold current density is expressed by the following equation:

$$J_{c0} = \frac{\alpha\gamma e M_S t_F H_{eff}}{\eta(\theta)\mu_0}, \tag{3}$$

where α is the Gilbert damping constant, γ is the gyromagnetic constant, e is the charge of electron, M_S is the saturation magnetization of the free layer, t_F is the thickness of the free layer, $\eta(\theta) = P/[2(1+P^2)\cos\theta]$ is the STT efficiency, P is the spin polarization factor, and θ is the angle of the magnetizations between the free and fixed layers ($\theta = 0$ for P state, π for AP state). H_{eff} is the effective field including the external applied field H_{ex}, anisotropy field H_K, demagnetization field H_d, and the stray or dipole field H_{st}.

3.4. TMR and temperature effects

TMR of the MTJ is expressed as $(R_{AP} - R_P)/R_P$, where R_{AP} and R_P are the antiparallel and parallel resistances of MTJ, respectively. Based on voltage- and temperature-dependent spin polarization factor P of magnetic materials, the voltage and temperature dependence of TMR can be captured using the modified Julliere's formula as follows:

$$\mathrm{TMR}(T,V) = \frac{2P_0^2(1-\alpha_{sp}T^{3/2})^2}{1-P_0^2(1-\alpha_{sp}T^{3/2})^2} \cdot \frac{1}{1+(V/V_0)^2}. \tag{4}$$

Here, P_0 is the polarization factor which can be experimentally determined by the low-bias TMR in R–V curves of MTJ, α_{sp} is the material-dependent empirical constant, and V_0 is the bias-voltage which can be determined by the high-bias features of TMR in the experimental observes [Fig. 1(b)].

3.5. Magnetization dynamics and LLG equation

Various studies have shown that the dynamical motion of a time-varying magnetization vector $M(t)$ under spin transfer torques can be well described by Landau–Lifshitz–Gilbert (LLG) equation as

$$\frac{1+\alpha^2}{\gamma} \cdot \frac{\mathrm{d}\boldsymbol{M}}{\mathrm{d}t} = -\boldsymbol{M} \times \boldsymbol{H}_{eff} - \alpha \cdot \boldsymbol{M} \times (\boldsymbol{M} \times \boldsymbol{H}_{eff}) + \frac{\hbar P J}{2e t_F M_S} \cdot \boldsymbol{M} \times (\boldsymbol{M} \times \boldsymbol{M}_p). \tag{5}$$

Here, γ is the gyromagnetic ratio, α is the Gilbert damping constant, $\hbar$ is the reduced Plank's constant, e is the electron charge, P is the spin polarization factor, J is the current density passing through the device, $\boldsymbol{H}_{eff}$ is the effective magnetic field including the different field components as mentioned above, M_S and t_F are the saturation magnetization and thickness of the magnetic free layer, $\boldsymbol{M}$ and $\boldsymbol{M}_p$ are the magnetization vectors of the free and fixed layers, respectively.

4. Spice simulation of STT-PMTJ

4.1. SPICE model framework

As inspired by the proposed SPICE-based LLG models for STT-MTJ in recent years,[28–31] we performed the substantial circuit simulation and analysis of the pMTJ devices strictly based on our experimental parameters to acquire the MTJ switching performance and its dependence on bias voltage V_{bias}, thickness of recording layer t_F (or magnetic anisotropy H_K), and damping constant α for guiding experiments to further optimize the device parameters for the development of MTJ. Figure 2 shows the SPICE model consisting of five sub-circuits: voltage-dependent magnetic anisotropy, LLG, STT, TMR, and temperature, similar to previous reports.[31] The simulation parameters of the STT-MTJ device are extracted from our experiments above and listed in Table 1.

Table 1. MTJ simulation parameters.

Parameters	Description	Default values
L_x	free layer length [nm]	56
L_y	free layer width [nm]	56
L_z	free layer thickness [nm]	1.46
t_c	critical thickness [nm]	1.5
t_{ox}	MgO thickness [nm]	1.4
M_{S0}	saturation magnetization @ 0 K (kA/m)	1000
P_0	polarization factor @ 0 K	0.8
α	magnetic damping factor	0.02
ξ	VCMA coefficient (fJ·V^{-1}·m^{-1})	33
RA	resistance-area product ($\Omega \cdot \mu m^2$)	10
T_0	initial temperature (K)	300
MA	perpendicular	1
State	parallel (0)/anti-parallel (1)	0/1

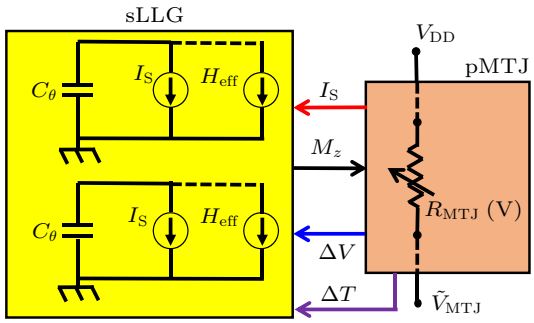


Fig. 2. SPICE model framework for modeling the MTJ-based devices in Fig. 1 based on the experimentally obtained parameters.

In our circuit simulation, a simple STT-MRAM cell consisting of a two-terminal MTJ in series with an access transistor is shown in Fig. 3(a). Consistent with our experimental devices, the two-terminal MTJ consists of a fixed layer, a barrier layer, and a free layer. In an STT-MRAM cell, the data is stored or coded by the magnetization direction of FL, which is controlled by the electric current passing through the MTJ cell. The bidirectional current is achieved by applying proper voltages to the bitline and the source line meanwhile keeping the corresponding access transistor on by applying an appropriate voltage to the word line. Figure 3(b) shows the representation of our experimental R–V curves. The R–V characteristics are well reproduced by using the modified Julliere's formula Eq. (4) with the fitting parameters $P_0 = 0.8$, $V_0 = 0.65$, and $\alpha_{sp} = 2 \times 10^{-5}$, as shown in Fig. 3(c).

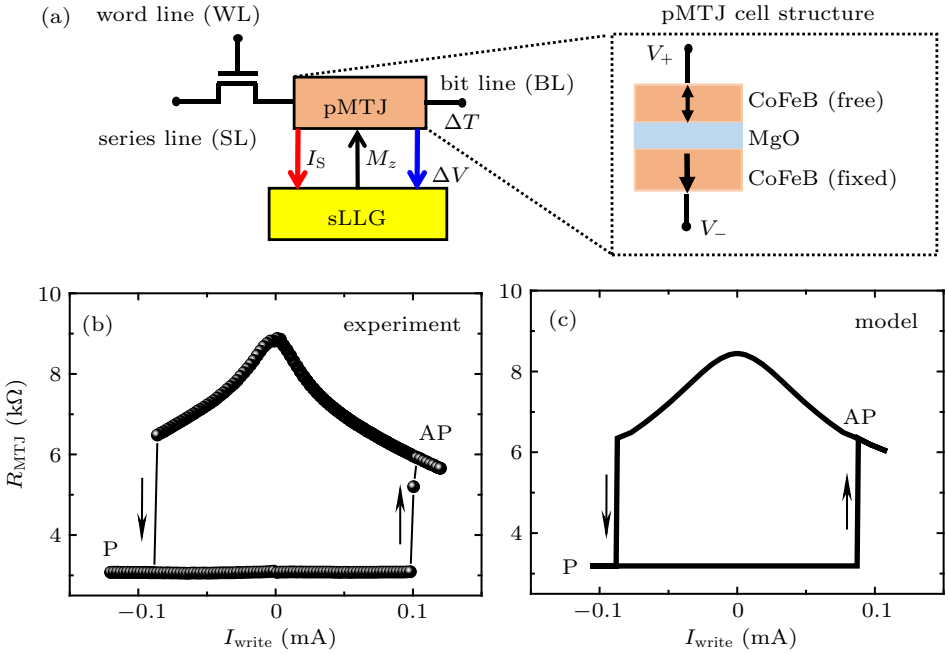


Fig. 3. The pMTJ-based STT-MRAM. (a) Spin-circuit modeling of an STT-pMRAM bit cell including spin-transfer-torque, voltage-controlled magnetic anisotropy, and temperature effects. (b) The experimental result of the bias current dependent TMR of our pMTJ device. (c) The simulation result of the modeling pMTJ-based STT-MRAM.

4.2. STT switching performance

Compared to the state-of-art of measurement technologies required in experimentally determining the ultra-fast switching time, the circuit simulation can easily access to STT-induced magnetization switching process by directly analyzing the time-domain circuit signal related to the magnetization of the free layer. The z-component of magnetization M_z as a function of time after applying a bias-voltage with different amplitudes on the MTJ cell is shown in Fig. 4. One can see that for both switching directions (P-to-AP and AP-to-P), the switching time τ corresponding to $M_z = 0$ decreases with the increase of the pulse amplitude. Since the studied magnetization switching in STT-MTJ is in the precessional switching regime, the switching is dominated by STT rather than temperature-dependent thermal activation effect. Based on the adiabatic precessional model, the switching time can be expressed as

$$\tau = \tau_0 \ln(\pi/2\theta_0)\left(\frac{V_0}{V - V_0}\right), \tag{6}$$

where τ_0 is the relaxation time, V_0 is the zero temperature instability voltage, and $\theta_0 = (k_B T/2E_b)^{1/2}$ is the initial angular deviation of the magnetization from its easy axis. According to the energy barrier $E_b = \mu_0 M_S V_F H_k/2$ discussed in Section 3 above, $\theta_0 = 0.105$ is obtained from our experimental results. Figures 4(c) and 4(d) show that the switching time obtained from the SPICE-based LLG model of STT-pMTJ for AP-to-P (P-to-AP) state can be well fitted by Eq. (6) with the fitting parameters $V_0 = 0.87$ (0.74) V and $\tau_0 = 0.35$ (0.72) ns, indicating the validation of the model. In addition, the switching time (inverse proportional to the switching voltage) of AP-to-P is shorter than that of P-to-AP, which is also consistent with our experimental observation and previous reports in pMTJ due to voltage-dependent magnetic anisotropy and polarization. Furthermore, the energy per write for a given pulse amplitude can be estimated by using $E_w = V_{bias}^2 \tau/R$. In practical operation, however, it should be noted that the bias voltage V_{bias} across the MTJ cells is related to the input pulse voltage V_{in} by $V_{bias} = 2V_{in}R_{AP/P}/(R_{AP/P} + Z_0)$ due to the mismatch between the high MTJ resistance and the $Z_0 = 50\ \Omega$ system impedance. $R_{AP} = 6.5\ \text{k}\Omega$ and $R_P = 3.2\ \text{k}\Omega$ are the resistances of antiparallel and parallel states of our MTJ devices, respectively. A minimum E_w for P-to-AP (AP-to-P) switching of 1.4 (0.5) pJ is estimated for the studied MTJ devices.

In addition to the switching current density, the switching time is another important parameter of STT-MRAM, because it is related to the write speed and power consumption of the device. Many previous theories, experiments, and numerical simulations showed that the switching current and time exhibit the complex dependence on multiple parameters, such as the saturation magnetization, the effective magnetic anisotropy, and damping constant, especially in the sub-100 nm scale STT-pMTJ. To get the relationship between switching performance and various material parameters for guiding and optimizing the design of STT-MRAM devices, we investigated the dependence of switching time on perpendicular magnetic anisotropy by varying the thickness t_F of the free layer, as shown in Fig. 5. As discussed in Fig. 4, the asymmetry of current-driven MTJ switching phenomena is observed under all four thicknesses studied. One can easily see that the switching time τ for both AP-to-P and P-to-AP decreases with reducing magnetic anisotropy because the iPMA decreases with the increase of free layer thickness t_F. Based on Eq. (6), we

can quantitatively estimate that the 40% reduction of iPMA K_i by increasing t_F from 0.8 nm to 1.4 nm causes about 47% reduction of average switching time $\langle\tau\rangle$ of AP-to-P and P-to-AP at bias voltage $V_{bias} = 2$ V. Although the reduction of $\langle\tau\rangle$ is degrading with increasing V_{bias}, it still has $\sim 30\%$ drop from $t_F = 0.8$ nm to 1.4 nm at $V_{bias} = 3.5$ V. Furthermore, Gilbert damping dependent switching time is also investigated, as shown in Fig. 6. Since the thin film CoFeB (~ 1 nm) as the free layer of the MTJ cell usually has a less than 0.1 damping constant (0.02 for our devices shown above), the study of damping-dependent τ is focused on the damping range of less than 0.1 for guiding the design of the practical STT-MRAM. Our results show that the damping constant has a significant influence on switching time τ during P-to-AP switching process, while a very weak effect on τ for AP-to-P.

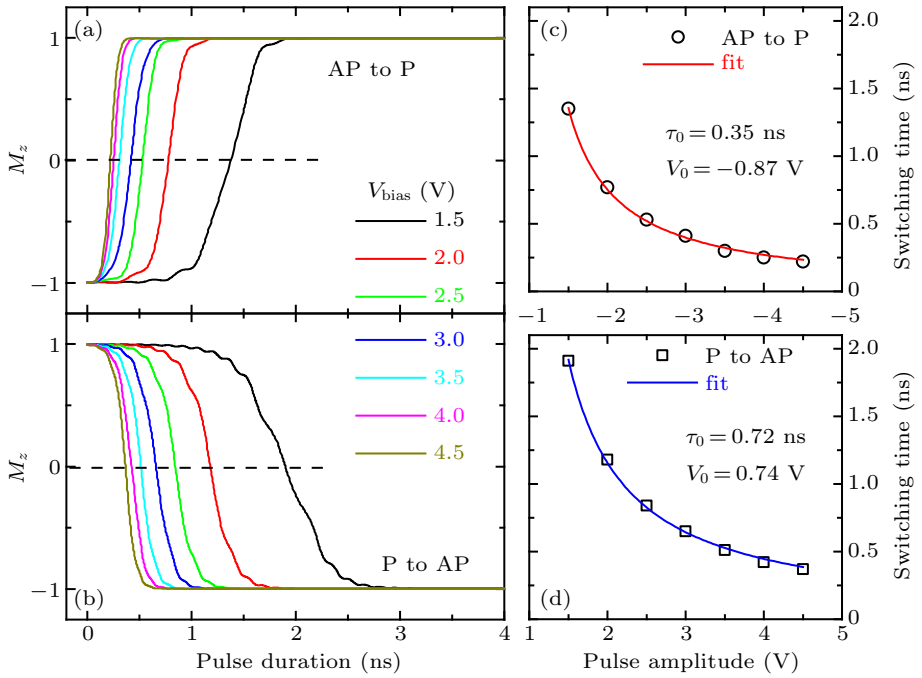


Fig. 4. Switching time performance at different bias voltage. (a) and (b) Switching process of M_z as a function of pulse duration time for AP-to-P state (a) and P-to-AP state (b) at various amplitudes of bias voltage pulse. (c) and (d) Switching time, defined at $M_z = 0$ (horizontal dished lines in (a) and (b)), as a function of pulse amplitude for AP-to-P state (c) and P-to-AP state (d). The symbols are the simulation results and the solid lines are the fitting curves with Eq. (6).

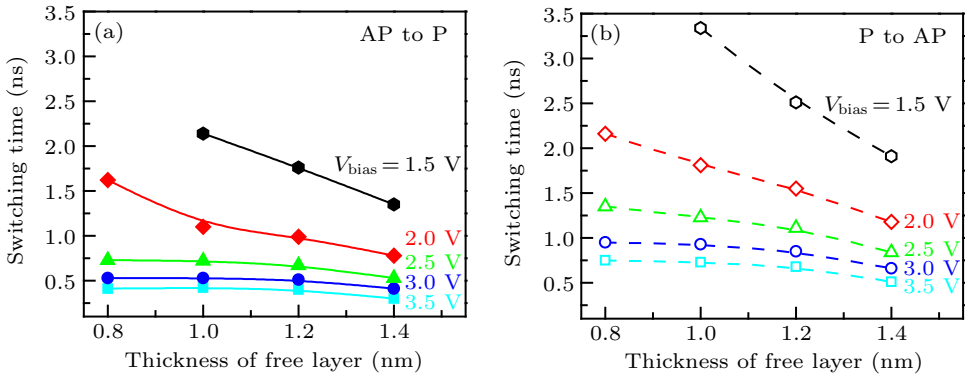


Fig. 5. Switching time as a function of the free layer thickness (perpendicular magnetic anisotropy K_i) for AP-to-P state (a) and P-to-AP state (b) at various amplitudes of bias voltages $V_{bias} = 1.5$ V, 2 V, 2.5 V, 3 V, and 3.5 V.

The conventional spin-torque nano-oscillators based on magnetic multilayer structures, spin-valve,[10] or MTJ;[32] recently developed spin-Hall nano-oscillators[26,33,34] based on nonmagnetic heavy metal and magnetic metal or insulator bilayer structure; and the magnetic auto-oscillators with highly current- and field-dependent frequency tunability, modulation, injection locking, and mutual synchronization have great potential applications as a class of miniaturized and ultra-broadband microwave signal generators for nanosensor and wireless communications, or as nanoscale spin-wave excitation sources for magnon-based devices.[25] The STNOs with the largest reported integrated output power have been presented in CoFeB-MgO-based MTJs due to their high TMR.[32] The studied pMTJ cells for STT-MRAM applications are also can be used as STNOs for RF electronics by adding an in-plane magnetic field at an appropriate current range. Figure 7

shows that current-driven STT can compete with the damping and sustain a stable magnetization procession at $V_{\rm bias} = 3$ V and in-plane field $H = 1500$ Oe. The representative auto-oscillation frequency spectra can be obtained by performing the fast Fourier transform (FFT) of the time-dependent z-component magnetization M_z depicted in Fig. 7(a). The FFT spectrum of M_z shows a primary peak at 3.3 GHz, which is below the frequency of ferromagnetic resonance 3.9 GHz, indicating that it is a localized mode. While the higher frequency ~ 6.6 GHz is its second harmonic mode. The frequency and power of magnetic nano-oscillators can be controlled by the applied current and magnetic field.

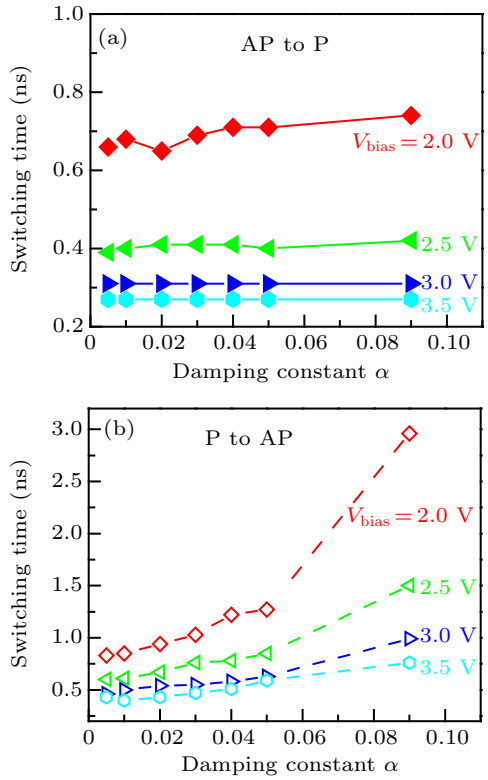


Fig. 6. Switching time τ vs. damping constant α for AP-to-P (a) and AP-to-P (b) at various amplitudes of bias voltages $V_{\rm bias} = 2$ V, 2.5 V, 3 V, and 3.5 V.

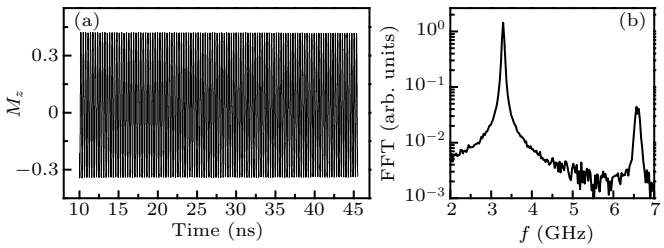


Fig. 7. STT sustained stable magnetization procession in pMTJ-based STNO. (a) Time trace of the normalized z-component magnetization M_z of the free layer in STNO at bias voltage $V_{\rm bias} = 3$ V and applied in-plane field $H = 1500$ Oe. (b) FFT spectrum of the free-running STNO with a foundational peak ~ 3.3 GHz and a second harmonic peak ~ 6.6 GHz.

5. Conclusion

We utilized stack structure MgO/CoFeB/Ta/CoFeB/MgO as the free layer of pMTJ, and achieved a high TMR ratio $\sim 190\%$ at room temperature, meanwhile keeping a well thermal stability factor ~ 73. Based on the experimental results and the extracted material parameters, we further estimated the STT-pMTJ switching performance including switching time and power, and their dependence on perpendicular magnetic anisotropy and damping constant of the free layer by SPICE-based circuit simulations including voltage-controlled magnetic anisotropy, spin-transfer-torque, and temperature effects. The observed TMR vs. current curves can be well reproduced by our circuit simulations, which validate the SPICE model of pMTJs. Our simulation results show that the pMTJ cells exhibit switching time less than 1 ns and write energies < 1.4 pJ; meanwhile the lower PMA and damping constant can further reduce the switching time at the studied range of damping constant $\alpha < 0.1$. Additionally, our results also demonstrate that the pMTJ cells could be easily transformed into spin-torque nano-oscillators from magnetic memory as microwave sources or detectors for telecommunication devices. Our results and methods suggest that the SPICE-based LLG model provides an efficient approach for the designers of spintronic devices to easily estimate key performance indicators of devices and optimize device and material parameters.

References

[1] Djayaprawiraa D D, Tsunekawa K, Nagai M, Maehara H, Yamagata S, Watanabe N, Yuasab S, Suzukic Y and Ando K 2005 *Appl. Phys. Lett.* **86** 092502

[2] Ikeda S, Hayakawa J, Lee Y M, Matsukura F, Ohno Y, Hanyu T and Ohno H 2007 *IEEE T. Electron Dev.* **54** 991

[3] Fu Q W, Zhou K Y, Chen L N, Xu Y B, Zhou T J, Wang D H, Chi K Q, Meng H, Liu B, Liu R H and Du Y W 2020 *Chin. Phys. Lett.* **37** 117501

[4] Makarov A, Windbacher T, Sverdlov V and Selberherr S 2016 *Semicond Sci. Tech.* **31** 113006

[5] Slonczewski J C 1996 *J. Magn. Magn. Mater.* **159** L1

[6] Berger L 1996 *Phys. Rev. B* **54** 9353

[7] Grollier J, Cros V, Hamzic A, George J M, Jaffres H, Fert A, Faini G, Ben Youssef J and Legall H 2001 *Appl. Phys. Lett.* **78** 3663

[8] Hayakawa J, Ikeda S, Miura K, Yarnanouchi M, Lee Y M, Sasaki R, Ichimura M, Ito K, Kawahara T, Takemura R, Meguro T, Matsukura F, Takahashi H, Matsuoka H and Ohno H 2008 *IEEE T. Magn.* **44** 1962

[9] Katine J A, Albert F J, Buhrman R A, Myers E B and Ralph D C 2000 *Phys. Rev. Lett.* **84** 3149

[10] Tsoi M, Jansen A G M, Bass J, Chiang W C, Tsoi V and Wyder P 2000 *Nature* **406** 46

[11] Liu H F, Ali S S and Han X F 2014 *Chin. Phys. B* **23** 077501

[12] Zhang Y J, Wang X B, Li Y, Jones A K and Chen Y R 2012 *Des. Aut. Test. Europe.* 1313

[13] Zeng Z M, Amiri P K, Rowlands G, Zhao H, Krivorotov I N, Wang J P, Katine J A, Langer J, Galatsis K, Wang K L and Jiang H W 2011 *Appl. Phys. Lett.* **98** 072512

[14] Sato H, Enobio E C I, Yamanouchi M, Ikeda S, Fukami S, Kanai S, Matsukura F and Ohno H 2014 *Appl. Phys. Lett.* **105** 062403

[15] Lee S E, Takemura Y and Park J G 2016 *Appl. Phys. Lett.* **109** 182405

[16] Song J, Ahmed I, Zhao Z Y, Zhang D L, Sapatnekar S S, Wang J P and Kim C H 2018 *IEEE J. Explor. Solid* **4** 76

[17] Weisheit M, Fahler S, Marty A, Souche Y, Poinsignon C and Givord D 2007 *Science* **315** 349

[18] Endo M, Kanai S, Ikeda S, Matsukura F and Ohno H 2010 *Appl. Phys. Lett.* **96** 212503

[19] Yoshida C, Noshiro H, Yamazaki Y, Sugii T, Furuya A, Ataka T, Tanaka T and Uehara Y 2016 *Aip Adv.* **6** 055816

[20] Wei H X, Lu Q F, Zhao S F, Zhang X Q, Feng J F and Han X F 2004 *Chin. Phys.* **13** 1553
[21] Han G C, Tran M, Sim C H, Wang J C, Eason K, Ter Lim S and Huang A H 2015 *J. Appl. Phys.* **117** 17B515
[22] Zhang L K, Fang B, Cai J L and Zeng Z M 2018 *Appl. Phys. Lett.* **112** 242408
[23] Shi S J, Ou Y X, Aradhya S V, Ralph D C and Buhrman R A 2018 *Phys. Rev. Appl.* **9** 011002
[24] Zheng C X, Chen H H, Zhang X L, Zhang Z Z and Liu Y W 2019 *Chin. Phys. B* **28** 037503
[25] Chen T S, Dumas R K, Eklund A, Muduli P K, Houshang A, Awad A A, Durrenfeld P, Malm B G, Rusu A and Akerman J 2016 *P IEEE* **104** 1919
[26] Li L Y, Chen L N, Liu R H and Du Y W 2020 *Chin. Phys. B* **29** 117102
[27] Yang M S, Fang L and Chi Y Q 2018 *Chin. Phys. B* **27** 098504
[28] Yamada K, Oomaru K, Nakamura S, Sato T and Nakatani Y 2016 *Appl. Phys. Lett.* **108** 042402
[29] Lim H, Lee S and Shin H 2014 *IEEE Electr Device L* **35** 193
[30] Torunbalci M M, Upadhyaya P, Bhave S A and Camsari K Y 2018 *IEEE T. Electron Dev.* **65** 4628
[31] Wang G D, Zhang Y, Wang J K, Zhang Z Z, Zhang K, Zheng Z Y, Klein J O, Ravelosona D, Zhang Y G and Zhao W S 2019 *IEEE T. Electron Dev.* **66** 2431
[32] Zeng Z M, Amiri P K, Krivorotov I N, Zhao H, Finocchio G, Wang J P, Katine J A, Huai Y M, Langer J, Galatsis K, Wang K L and Jiang H W 2012 *Acs Nano* **6** 6115
[33] Liu R H, Chen L N, Urazhdin S and Du Y W 2017 *Phys. Rev. Appl.* **8** 021001
[34] Chen L N, Urazhdin S, Du Y W and Liu R H 2019 *Phys. Rev. Appl.* **11** 064038